$Al_{0.78}Sc_{0.22}N$ Lamb Wave Contour Mode Resonators

Zhifang Luo, *Student Member, IEEE*, Shuai Shao, and Tao Wu, *Member, IEEE*

***Abstract*— This article presents the lamb wave contour mode resonators (CMRs) based on 22% aluminum scandium nitride (AlScN) thin film with λ of 12–24 μm, and operating in S_0 mode. We report the design, fabrication, and characterization of 500 nm-thick AlScN CMRs, which take advantage of optimized stress control of co-sputtered AlScN thin films and vertical inductively coupled plasma (ICP) etching profile. The experimental results are compared to theoretical predictions by finite element analysis (FEA). All $Al_{0.78}Sc_{0.22}N$ devices show excellent agreement with simulations in piezoelectric coupling using modified AlScN film parameters. The best $Al_{0.78}Sc_{0.22}N$ CMR has achieved an electromechanical coupling coefficient (k_t^2) of 5.24% and loaded quality factor (Q) of 1219 with an operating frequency at approximately 300 MHz, which exhibits a high Figure-of-Merit (FoM) of 63.88 in piezoelectric microelectromechanical system (MEMS) lamb wave CMR. This article also presents the co-sputtering characteristics of the AlScN thin films under N_2 gas to achieve low-stress and high-quality piezoelectric materials, and the etching optimization of high concentration Sc doping aluminum nitride (AlN) thin films under $Cl_2/BCl_3/Ar$ chemistry to obtain record profile angle of 77°, high selectivity of 1:1 with SiO_2 hard mask.**

***Index Terms*— Aluminum scandium nitride (AlScN), contour mode resonator (CMR), lamb wave, microelectromechanical system (MEMS).**

I. Introduction

PIEZOELECTRIC microelectromechanical system (MEMS) transducers have been widely employed in radio frequency (RF) technologies [1]–[4]. Many piezoelectric devices have been investigated such as surface acoustic wave (SAW) [5], thin film bulk acoustic resonators (FBAR) [6], [7], and lamb wave contour mode resonators (CMRs) [8], [9]. Among these, aluminum nitride (AlN)-based CMRs have been studied as one of the most promising approaches due to its chip-scale multiple operating frequencies and high-performance resonators. In the past decades, different kinds of piezoelectric thin film materials have been reported and characterized, such as zinc oxide (ZnO) [10], [11], AlN [12], [13], doped-AlN [14], [15], and lithium niobate (LN) [16], [17]. Aluminum scandium nitride (AlScN) thin films-based MEMS resonators have been proved to achieve high k_t^2 utilizing a CMOS compatible sputtering process [18]–[20]. With a higher Sc concentration in doping AlN films, d_{33} and d_{31} piezoelectric coefficients both enhance significantly. However, Park *et al.* [21] state that the stress of high concentration Sc doping thin films is hard to control, and the difficultly of AlScN dry etching adds further challenge to achieving high-performance devices.

For piezoelectric resonators, Figure-of-Merit (FoM) ($k_t^2 \cdot Q$) is a key parameter to quantify the performance of the devices. k_t^2 is defined as the efficiency to convert energy from the electric domain to the mechanical domain. Quality factor Q is seen as the ratio of stored energy and lost energy in resonance. In the part of fabrication, the relatively poor crystal quality of AlN and AlScN thin films results in limited k_t^2 and Q [22], [23]. Then, the boundary profile of resonating structure plays an important role in lamb wave propagation and piezoelectric coupling, thus the profile is essential for k_t^2 of resonators. For the design of the device, there are several loss mechanisms in CMRs, such as the anchor loss and the damping loss from the resonators, while the anchor loss is the main part of the resonator. In addition, the choice of top electrode metal influences the k_t^2 a lot. Currently, less work investigates the fabrication process with theoretical and experimental results, particularly the deposition and etching of piezoelectric thin film with Sc concentration over 20%, as well as the design of the devices simultaneously. We believe that our work can be seen as a useful guideline utilizing more physics-based discussion.

In this work, the fabrication challenges and designs of CMRs based on $Al_{0.78}Sc_{0.22}N$ thin film are solved. About 22% Sc-doped AlN thin films are deposited using CMOS compatible co-sputtering process with great crystalline quality and stress control. Then, optimized inductively coupled plasma (ICP) dry etching is utilized to achieve a great boundary profile. Moreover, we provide simulation to design the optimal anchor shape of resonators. Finally, high-performance $Al_{0.78}Sc_{0.22}$ N CMRs are fabricated, achieving a high FoM of

Manuscript received 8 November 2021; accepted 9 December 2021. Date of publication 16 December 2021; date of current version 2 November 2022. This work was supported in part by the National Natural Science Foundation of China under Grant 61874073; in part by the Natural Science Foundation of Shanghai under Grant 19ZR1477000; and in part by the device fabrication and characterization support from the ShanghaiTech Quantum Device Laboratory (SQDL) and the Analytical Instrumentation Center, School of Physical Sciences and Technology, ShanghaiTech University, under Grant SPST-AIC10112914. *(Corresponding author: Tao Wu.)*

The authors are with the School of Information Science and Technology, ShanghaiTech University, Shanghai 201210, China, also with the Shanghai Institute of Microsystem and Information Technology, Chinese Academy of Sciences, Shanghai 200050, China, and also with the University of Chinese Academy of Sciences, Shijingshan, Beijing 100049, China (e-mail: luozhf@shanghaitech.edu.cn; shaoshuai@shanghaitech.edu.cn; wutao@shanghaitech.edu.cn).

Digital Object Identifier 10.1109/TUFFC.2021.3136337

1525-8955 © 2021 IEEE. Personal use is permitted, but republication/redistribution requires IEEE permission.
See https://www.ieee.org/publications/rights/index.html for more information.

Authorized licensed use limited to: ShanghaiTech University. Downloaded on June 01,2023 at 08:48:10 UTC from IEEE Xplore. Restrictions apply.

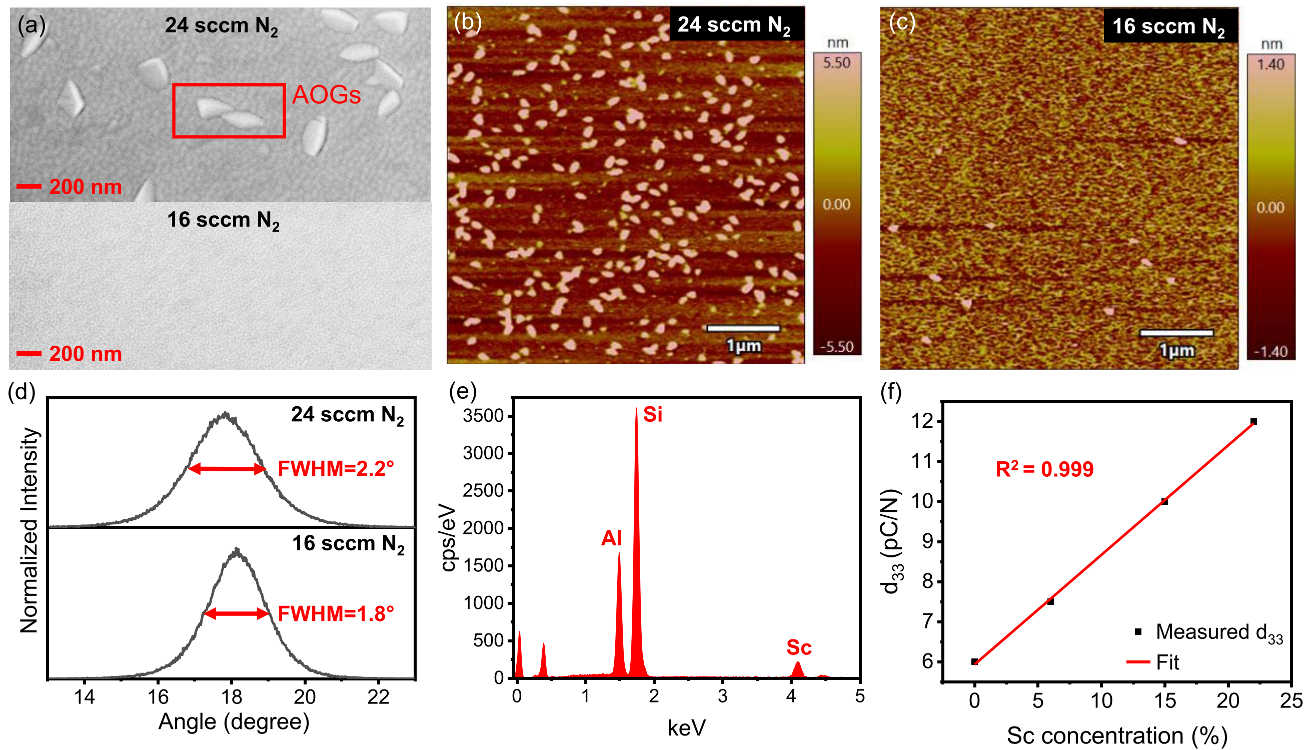

Fig. 1. SEM top view of (0002) oriented $Al_{0.78}Sc_{0.22}N$ surface. (a) Top: under 24 sccm flow rate of N_2, bottom: under 16 sccm flow rate of N_2. AFM height image of the $Al_{0.78}Sc_{0.22}N$ film surface under (b) 24 sccm flow rate of N_2 and (c) 16 sccm flow rate of N_2. (d) XRD rocking curve of $Al_{0.78}Sc_{0.22}N$ thin film, top: under 24 sccm flow rate of N_2, bottom: under 16 sccm flow rate of N_2. (e) EDS spectrum for Sc concentration measurement of $Al_{0.78}Sc_{0.22}N$ thin film. (f) Measured and fitted d_{33} piezoelectric coefficient of $Al_{0.78}Sc_{0.22}N$ thin film as a function of Sc concentration.

63.88 in lamb wave CMRs. Such $Al_{0.78}Sc_{0.22}N$ thin film-based lamb wave CMRs are of great significance in RF front-end and transducer application.

II. Fabrication

There are two challenging processes during fabrication steps, $Al_{0.78}Sc_{0.22}N$ co-sputtering and $Al_{0.78}Sc_{0.22}N$ ICP etching. As a metastable state, AlScN thin film requires more stringent growth conditions than AlN thin film. For device processing, the primary considerations are crystal quality and film stress, which determine the film robustness and device performance, respectively. However, these problems are more significant in high concentration scandium doping thin films. The AlScN film with good crystal orientation tends to use a lower pressure growth environment and tends to grow a thin film with compressive stress, which makes the film very easy to bend or even break during release. In our work, we have studied the AlScN film co-sputtering process and optimized the sputtering gas and power to solve this problem.

A 0.5 μm (0002) polar $Al_{0.78}Sc_{0.22}N$ thin film is deposited using the EVATEC CLN200 MSQ system. The chemical reaction during the sputtering process can be expressed as

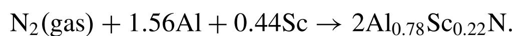

$$N_2(\text{gas}) + 1.56\text{Al} + 0.44\text{Sc} \rightarrow 2\text{Al}_{0.78}\text{Sc}_{0.22}\text{N}.$$

Compared to the AlN, the $Al_{0.78}Sc_{0.22}N$ thin film is formed by replacing 22% Al atoms with Sc atoms. Such reactions involve bond breaking and making. The bond energy (BE) of Al-N is $\leq 365 \pm 15$ kJ/mol, and that of Sc-N is 464 ± 84 kJ/mol [24]. It means that about 27% more energy is needed to make each Sc-N bond than the Al-N bond. For $Al_{0.78}Sc_{0.22}N$, 6% more energy is required. The efficiency and quality of making co-sputtered highly rely on the sputtering energy. Relatively high energy is a benefit for uniform energy transfer and reactant flow on the substrate, and then aligning the crystal greater [25]. Tuning the sputtering pressure is a vital way in AlScN deposition to modulate sputtering energy. By adjusting the sputtering gas, the deposition pressure is varied. The $Al_{0.78}Sc_{0.22}N$ thin films are obtained at 1000 W Al and 450 W Sc with two Al and Sc targets, respectively. Average stress of approximately -128 MPa on a 4 in wafer has been achieved using an 8 in carrier substrate by adequately tuning the flow rate of N_2 gas. The surface morphology of $Al_{0.78}Sc_{0.22}N$ films is measured by scanning electron microscopy (SEM) Zeiss Gemini300. Under the 24 sccm flow rate of N_2, many abnormal orientation grains (AOGs) with a grain size of nearly 300 nm can be observed on the surface, while the grain size increases and grain growth is more disordered as indicated in the top of Fig. 1(a). More AOGs occur at the AlScN surface when using the same deposition conditions compared to the AlScN thin films with lower concentrations. AOGs will attenuate the piezoelectric response and then decrease the performance of devices. In order to obtain high-quality $Al_{0.78}Sc_{0.22}N$ thin films, the flow rate of N_2 is reduced from 24 to 16 sccm. When the flow rate of N_2 decreases, the total pressure in the chamber drops and sputtering energy increases. The experimental results are consistent with our theory.

Authorized licensed use limited to: ShanghaiTech University. Downloaded on June 01,2023 at 08:48:10 UTC from IEEE Xplore. Restrictions apply.

A cleaner film surface is achieved when decreasing the flow rate of N_2, as shown at the bottom of Fig. 1(a). Fig. 1(b) and (c) show the surface topography of $Al_{0.78}Sc_{0.22}N$ thin films under different flow rates of N_2 by Asylum Research MFP Origin+ atomic force microscopy (AFM). AFM technique has the advantage of better characterizing the roughness of films. A large amount of AOGs can be found at the $Al_{0.78}Sc_{0.22}N$ thin films under a 24 sccm flow rate of N_2, and AOGs occupy almost half of the surface of films. When decreasing the flow rate of N_2, the surface roughness RMS value of $Al_{0.78}Sc_{0.22}N$ thin films is reduced from 5.50 to 1.40 nm. Due to the higher deposition rate of AOGs than normal AlScN crystal grains, the much lower amount of AOGs at the surface results in better uniformity. Compared to the $Al_{0.78}Sc_{0.22}N$ thin film under a 24 sccm flow rate of N_2, the surface morphology of film under the 16 sccm flow rate of N_2 shows a much cleaner and more uniform spectrum. The crystal orientation is measured by X-ray diffraction (XRD) from PANalytical[1] Empyrean. A decrease in the flow rate of N_2 results in a reduction of the FWHM value of $Al_{0.78}Sc_{0.22}N$ thin films from 2.2° to 1.8°, as illustrated in Fig. 1(d). The Sc concentration of the AlScN films is characterized and extracted by the energy-dispersive X-ray spectrum (EDS) of the Oxford AZtec system, as indicated in Fig. 1(e). The dispersive energies of each atom in the stack are measured and shown in the graph; since the AlScN films are deposited on the silicon wafer, the X-ray energy can be transmitted to the silicon. Higher dispersive energy illustrates a relatively higher concentration. We also investigate the dependence of d_{33} piezoelectric coefficient of $Al_{1-x}Sc_xN$ ($0 \leq x \leq 22\%$) on Sc concentrations. With increasing the concentration of Sc, the value of d_{33} increases linearly; the R^2 value is 0.999. The d_{33} piezoelectric coefficient increases by 0.274 ± 0.005 for every 1% increase in Sc concentration. When the Sc concentration is 22%, the thin film exhibits the d_{33} piezoelectric coefficient of 12 pC/N, which is a 2× improvement in the piezoelectric response with respect to pure AlN, as shown in Fig. 1(f).

Overall, under the 16 sccm flow rate of N_2, there are no obvious AOGs, the roughness of the film surface is 1.40 nm, and XRD FWHM is 1.8°, as illustrated in the bottom of Fig. 1(a), (c), and (d). While, under a 24 sccm flow rate of N_2, AlScN thin films show massive AOGs with much rougher surface and worse c-axis orientation, as seen in the bottom of Fig. 1(a), (b), and (d). Compared to the films under 24 sccm N_2, the grains of $Al_{0.78}Sc_{0.22}N$ thin films under 16 sccm N_2 are better aligned in the c-axis. The polarity of $Al_{0.78}Sc_{0.22}N$ thin films is improved by increasing sputtering energy. Meanwhile, the denseness of grain is directly affected by the sputtering energy. In order to deposit high concentration, Sc doping thin films with high quality and higher sputtering energy is needed to make the grains aligned denser.

$Al_{0.78}Sc_{0.22}N$ ICP etching is another challenge in order to achieve high-performance AlScN lamb wave resonators. ICP etching is an anisotropic etching process. Such a process is essential for lamb wave resonators to define device dimensions and release windows. AlN ICP etching process with $Cl_2/BCl_3/N_2$ mixed gas has been studied in our previous work [26]. Unfortunately, the previous experience on AlN is not suitable for the etching of AlScN thin film, especially for the high concentration of scandium doping. Etch rate, selectivity, and profile are the three key parameters we should be concerned about. After scandium doped in the AlN thin film, such three parameters all declined to the unacceptable values. The dimensions and release windows of resonators can hardly be defined using similar recipes. The $Al_{0.78}Sc_{0.22}N$ ICP etching mechanism with $Cl_2/BCl_3/Ar$ can be expressed by the following etching model.

1) *Step 1 (Non-Dissociative Adsorption):*

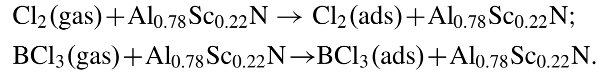

$$Cl_2(gas)+Al_{0.78}Sc_{0.22}N \rightarrow Cl_2(ads)+Al_{0.78}Sc_{0.22}N;$$
$$BCl_3(gas)+Al_{0.78}Sc_{0.22}N \rightarrow BCl_3(ads)+Al_{0.78}Sc_{0.22}N.$$

2) *Step 2 (Dissociative Adsorption):*

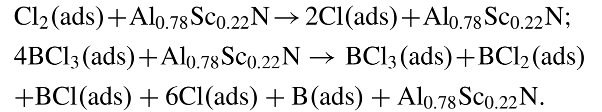

$$Cl_2(ads)+Al_{0.78}Sc_{0.22}N \rightarrow 2Cl(ads)+Al_{0.78}Sc_{0.22}N;$$
$$4BCl_3(ads)+Al_{0.78}Sc_{0.22}N \rightarrow BCl_3(ads)+BCl_2(ads) +BCl(ads)+6Cl(ads)+B(ads)+Al_{0.78}Sc_{0.22}N.$$

3) *Step 3 (Formation of Product Molecule):*

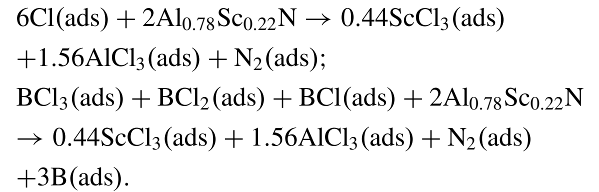

$$6Cl(ads)+2Al_{0.78}Sc_{0.22}N \rightarrow 0.44ScCl_3(ads) +1.56AlCl_3(ads)+N_2(ads);$$
$$BCl_3(ads)+BCl_2(ads)+BCl(ads)+2Al_{0.78}Sc_{0.22}N \rightarrow 0.44ScCl_3(ads)+1.56AlCl_3(ads)+N_2(ads) +3B(ads).$$

4) *Step 4 (Desorption of Product Molecule):*

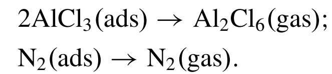

$$2AlCl_3(ads) \rightarrow Al_2Cl_6(gas);$$
$$N_2(ads) \rightarrow N_2(gas).$$

5) *Step 5 (Residue Removal):*

$$B(ads)+3Cl(ads) \rightarrow BCl_3(gas).$$

The first two steps of the $Al_{0.78}Sc_{0.22}N$ etching model are similar to that of AlN. First, Cl_2 and BCl_3 in the gas phase are non-dissociatively absorbed on the surface. Then, Cl_2 and BCl_3 in the gas phase are dissociated into Cl, and BCl_2, BCl, Cl, B, respectively, and are absorbed on the surface of $Al_{0.78}Sc_{0.22}N$. In step 3 of formation of product molecule, absorbed BCl_3, BCl_2, BCl, Cl, and B react with $Al_{0.78}Sc_{0.22}N$. The chemical reaction products absorbed $AlCl_3$ and $ScCl_3$ with by-products of absorbed B and N_2. In step 4 of desorption, the $AlCl_3$ product is desorbed and sublimated, and then the Al_2Cl_6 dimer in the gas phase is generated. In step 5 of residue removal, the by-product of B is reacted with Cl and converts BCl_3 into gas. In the whole etching process we discussed earlier, the $ScCl_3$ product always exists at the surface being etched once in generation. Unlike $AlCl_3$, $ScCl_3$ product cannot be desorbed and sublimated. The sublimation temperature of absorbed $ScCl_3$ is higher than 900 °C, while it is only 100 °C for absorbed $AlCl_3$. Since the high sublimation temperature of $ScCl_3$, it can rarely be removed from the etching surface.

Existing $ScCl_3$ enormously affects the AlScN film etching, especially for high Sc doping concentration films. Using a similar Cl-based gas recipe, the etch rate and selectivity of $Al_{0.78}Sc_{0.22}N$ thin films drop by almost 70%, the profile angle

Authorized licensed use limited to: ShanghaiTech University. Downloaded on June 01,2023 at 08:48:10 UTC from IEEE Xplore. Restrictions apply.

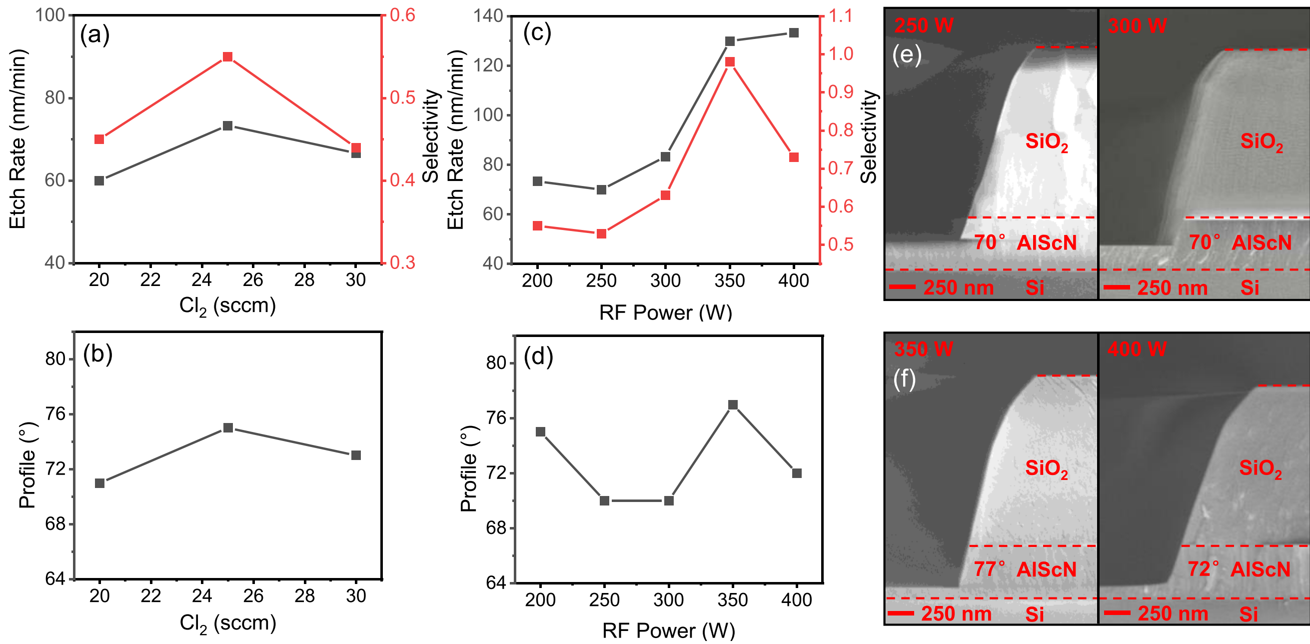

Fig. 2. ICP etch rate, selectivity, and profile versus (a) and (b) flow rate of Cl_2 and (c) and (d) RF power. SEM cross-section view of AlScN etching results with RF power of (e) 250 W, 300 W; and (f) 350 W, 400 W. Red dashed lines are guided for the eye.

drops by 40% compared to pure AlN thin films. Due to limited etch rate and poor profile angle, the quality factor Q and electromechanical coupling k_t^2 of AlScN lamb wave resonators would drop significantly [27]. Moreover, due to the much lower etch selectivity, the design of devices may be restricted by the etching process. For AlScN piezoelectric thin film, the thicker film usually shows better piezoelectricity. In this work, several etching parameters, such as flow rate of Cl_2 and RF power, have been studied to better understand the ICP etching mechanism on $Al_{0.78}Sc_{0.22}N$ film, and then a good vertical profile over 75° has been achieved.

The flow rate of Cl_2 and the value of RF power are the two essential etching parameters. The former decides the amount of etchant, and the latter determines the plasma energy. Fig. 2(a) and (b) show the etch rate, selectivity, and profile as a function of the flow rate of Cl_2 under 550 W ICP power, 200 W RF power, 5 Pa pressure, and BCl_3/Ar = 30/20 sccm, respectively. Cl_2 is the main etching gas, thus it is necessary to discuss the influence of Cl_2. According to the etching model, absorbed Cl_2 reacts with $Al_{0.78}Sc_{0.22}N$ and generates $AlCl_3$, $ScCl_3$. As the proportion of Cl_2 continues to increase, the etching rate and selectivity are fluctuated and cannot be further improved because of the deposition of $ScCl_3$, which is much less volatile than $AlCl_3$ and limits the chemical reaction between Cl_2 and $Al_{0.78}Sc_{0.22}N$. The etch profile slightly increases from about 71° to 73°. This is because the increasing Cl_2 gas flow can improve the anisotropy of etching. Fig. 2(c) and (d) illustrate the etch rate, selectivity, and profile as a function of RF power under 550 W ICP power, 5 Pa pressure, and Cl_2/BCl_3/Ar = 25/30/20 sccm. RF power is a critical parameter in controlling plasma bombardment energy. As we have discussed earlier about Cl_2 flow rate, the etching process is mainly restricted by the redeposition of $ScCl_3$. Due to the high sublimation temperature of $ScCl_3$, increasing physical bombardment energy may be the most straightforward approach to remove the absorbed $ScCl_3$ molecular. The energy of the physical bombardment to the sample increases when increasing the RF power. The increase in RF power not only removes the $ScCl_3$, but also etches the film by pure physical bombardment, so that both the chemical and physical processes are enhanced. The etching results are consistent with our theory. As the RF power increases from 200 to 350 W, the etching rate increases from 70 to 130 nm/min dramatically, thanks to the enhanced chemical and physical process. Then it slightly reaches 133 nm/min under RF power of 400 W. The selectivity also sharply increases to nearly 1:1 at 350 W RF power. The enhanced physical and chemical processes both act at the etch rate of $Al_{0.78}Sc_{0.22}N$, but for SiO_2, only the physical bombardment promotes etch rate. In other words, the etch rate of $Al_{0.78}Sc_{0.22}N$ increases faster than the mask, so the selectivity increases. However, when we further increase the RF power, the selectivity decreases significantly to 0.7:1. Such phenomenon can be explained by the too strong physical bombardment by the heavy atoms or molecules. Due to the higher hardness of the AlScN thin film, the SiO_2 hard mask is more likely to be consumed. Thus, the selectivity is dropped. As for the profile, the values are fluctuated and remained as the great anisotropy of etching. The profile of the SiO_2 hard mask is also a restriction for achieving a further improved profile. Fig. 2(e) and (f) show the SEM cross-section view of etching results of $Al_{0.78}Sc_{0.22}N$ thin film by using LICP-200 (Leuven Instrument). They are both captured under the same etching conditions, except for RF power. The higher RF power results in a higher etch rate, which can be seen from the thickness of remained films. Only 70° of the profile is obtained under 250 W RF power. The profile achieves a 77° under

Authorized licensed use limited to: ShanghaiTech University. Downloaded on June 01,2023 at 08:48:10 UTC from IEEE Xplore. Restrictions apply.

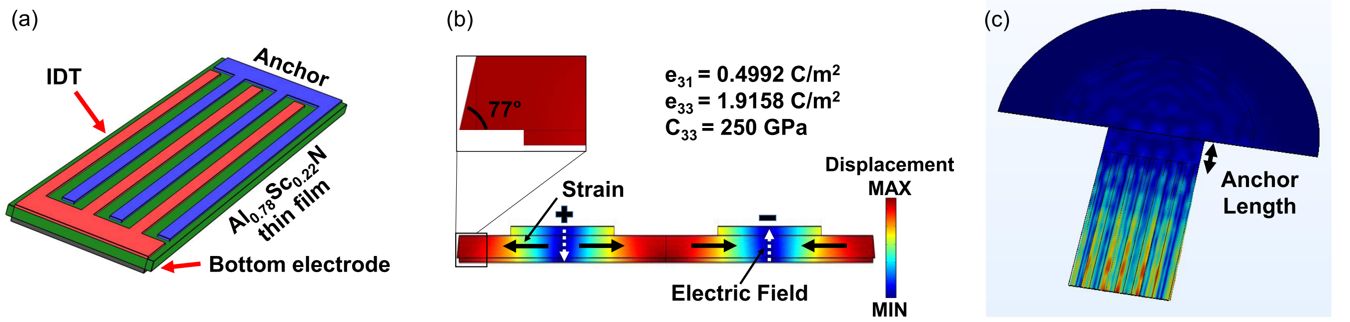

Fig. 3. (a) Illustrations of the $Al_{0.78}Sc_{0.22}N$ CMR. (b) Displacement FEA simulation of the $Al_{0.78}Sc_{0.22}N$ CMR. (c) Simulated displacement fields of the $Al_{0.78}Sc_{0.22}N$ CMR.

350 W RF power, while the etching surface has no residues. Fig. 2(f) clearly shows the reduction in selectivity under 400 W RF power by consuming more hard mask. With the higher RF power, the slope of the hard mask and $Al_{0.78}Sc_{0.22}N$ film both achieved much smoother morphologies, which is constant with our theory.

According to these findings, the recipe of 550 W ICP power, 350 W RF power, 5 Pa pressure, and $Cl_2/BCl_3/N_2 = 25/30/20$ sccm is used in the fabrication of $Al_{0.78}Sc_{0.22}N$ CMRs.

III. Simulations and Experiments

Material constants of $Al_{0.78}Sc_{0.22}N$ used in finite element analysis (FEA) simulations are calculated by the equation demonstrated by Caro *et al.* [28]

$$e_{15} = -0.367(1-x) - 0.435x + 0.417x(1-x) \quad (1)$$
$$e_{31} = -0.424(1-x) - 0.286x - 0.615x(1-x) \quad (2)$$
$$e_{33} = 1.449(1-x) + 8.182x - 5.912x(1-x) \quad (3)$$
$$C_{11} = 378.8(1-x) + 263.9x - 210.3x(1-x) \quad (4)$$
$$C_{12} = 128.9(1-x) + 185.1x - 61.9x(1-x) \quad (5)$$
$$C_{13} = 96.1(1-x) + 121.5x + 78.9x(1-x) \quad (6)$$
$$C_{33} = 357.5(1-x) - 51.3x - 101.4x(1-x) \quad (7)$$
$$C_{44} = 112.4(1-x) + 159.0x - 137.3x(1-x) \quad (8)$$

where e_{ij} is the piezoelectric coefficient, C_{ij} is the elastic constant. For $x = 0.22$, the $e_{15} = -0.3104$ C/m², $e_{31} = -0.4992$ C/m², $e_{33} = 1.9158$ C/m², $C_{11} = 317$ GPa, $C_{12} = 131$ GPa, $C_{13} = 115$ GPa, $C_{33} = 250$ GPa, $C_{44} = 99$ GPa, calculated by (1)–(8).

As shown in Fig. 3(a), an $Al_{0.78}Sc_{0.22}N$ CMR consists of a bottom electrode, $Al_{0.78}Sc_{0.22}N$ thin film, and interdigital (IDT) electrodes, which are connected to the pad by anchors. Fig. 3(b) shows the S_0 mode shape of $Al_{0.78}Sc_{0.22}N$ lamb wave CMR, illustrating the symmetric deformation shape in the $Al_{0.78}Sc_{0.22}N$ layer. The floating metal is utilized to improve the deposition of $Al_{0.78}Sc_{0.22}N$ thin film, and offer better confinement of the electric field in the resonant region of CMRs. When AC signal is applied to the input port, the electric field through the whole $Al_{0.78}Sc_{0.22}N$ thin film in the direction of thickness causes an in-plane deformation of the structure, and excites the CMRs in a vibration pattern of contour extensional mode in the direction of width. Due to the direct piezoelectric effect, the charge is generated and absorbed by the adjacent sensing electrodes. The thickness to wavelength ratio h/λ of the CMR equals 0.0119–0.4167, where h is the thickness of piezoelectric $Al_{0.78}Sc_{0.22}N$ thin film of 0.5 μm, and wavelength λ varies from 12 to 24 μm in these designs. The etched boundary profile of CMRs, approximately 77°, has been taken into consideration and the insert shows the simulation parameters used in FEA. Besides the influence of the ICP etching profile on the value of k_t^2, the design of the anchor is also essential for the Q factor of devices. We have studied the anchor dimension to minimize the loss of $Al_{0.78}Sc_{0.22}N$ CMRs in COMSOL Multiphysics[1]. FEA based on the perfectly matched layer (PML) is used to simulate the displacement fields of resonators [29], [30]. Fig. 3(c) shows the displacement fields of 24 μm wavelength $Al_{0.78}Sc_{0.22}N$ CMR utilizing PML-based FEA. The displacement fields in the piezoelectric plate are much less than those in the vibration region. In other words, when using a designed anchor with 23 μm length, there are few energies leaked in the piezoelectric plate via anchor.

Fig. 4(a) illustrates the admittance response and Q factor of $Al_{0.78}Sc_{0.22}N$ CMRs with different anchor lengths. The theoretical admittance response of devices is simulated by 3-D frequency domain analysis. The best performance in the $Al_{0.78}Sc_{0.22}N$ CMRs is found for an anchor length of 23 μm. The Q value is up to 3496.1, which is 54% higher compared to the device with an anchor length of 28 μm. In order to characterize the energy transduction efficiency between the electrical and mechanical domains of $Al_{0.78}Sc_{0.22}N$ CMRs, the intrinsic coupling coefficient k^2 of it is simulated in Fig. 4(b). The k^2 can be estimated by the Adler's approach

$$k^2 = \frac{\upsilon_0^2 - \upsilon_m^2}{\upsilon_0^2} \quad (9)$$

where the υ_0 is the phase velocity for a free surface, and υ_m is the phase velocity for a metalized surface by IDT. These two parameters are extracted from the nulls and poles of the effective permittivity [31]. As can be seen in Fig. 4(b), the S_0 mode has much higher k^2 than that of A_0 mode, due to the much larger phase velocities difference $\delta\upsilon$. For the S_0 mode we are interested in, thinner normalized thickness h/λ achieves higher k^2, especially when h/λ is less than 0.2. Unlike k^2, the

Authorized licensed use limited to: ShanghaiTech University. Downloaded on June 01,2023 at 08:48:10 UTC from IEEE Xplore. Restrictions apply.

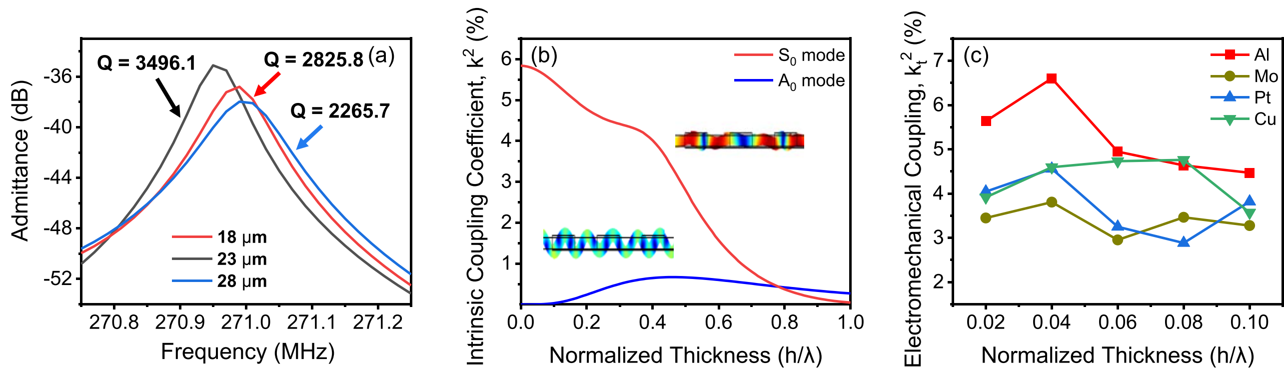

Fig. 4. (a) Simulated admittance response and Q value of $Al_{0.78}Sc_{0.22}N$ CMRs varying the length of the anchor. (b) Simulated dispersive intrinsic coupling coefficient k^2 of the S_0 and A_0 modes of $Al_{0.78}Sc_{0.22}N$ CMRs. (c) Simulated k_t^2 of $Al_{0.78}Sc_{0.22}N$ CMRs operating at S_0 mode with different metals.

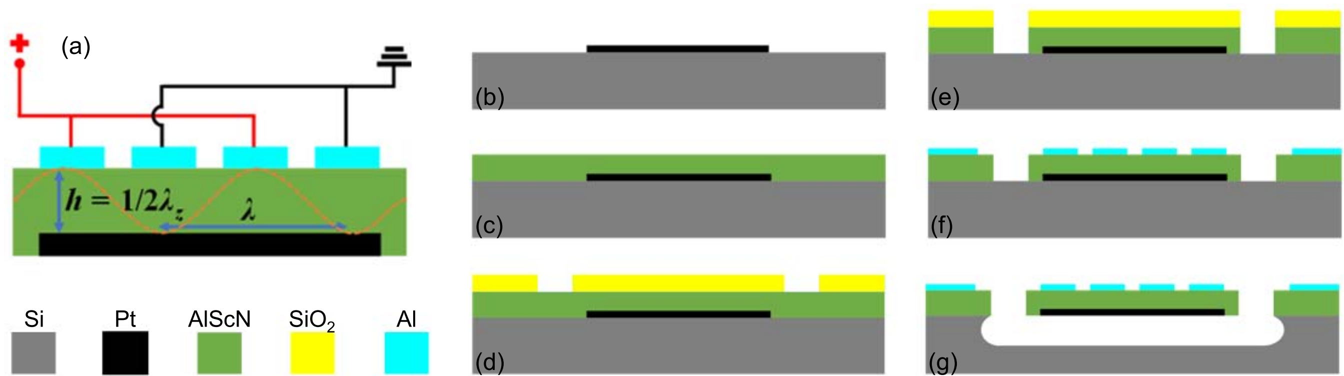

Fig. 5. (a) Schematic drawing of $Al_{0.78}Sc_{0.22}N$ CMRs and its electrical connection to the top interdigitated electrodes made of Al. (b)–(g) Process flow of $Al_{0.78}Sc_{0.22}N$ CMRs.

effective electromechanical coupling coefficient k_t^2 is extracted from the resonant and anti-resonant frequencies of resonators. The k_t^2 of CMRs is defined as

$$k_t^2 = \frac{\pi^2}{8} \times \frac{(f_a^2 - f_r^2)}{f_a^2} \quad (10)$$

where f_r is resonant frequency and f_a is anti-resonant frequency. The intrinsic coupling coefficient k^2 and the effective electromechanical coupling coefficient k_t^2 can both indicate the efficiency of energy transduction. According to the acoustic loss in metallization, the choice of metal used in IDT is essential for device performance. Accordingly, the influences of different metals on k_t^2 are characterized using FEA simulations. As shown in Fig. 4(c), when the thickness of metal is 200 nm, the IDT electrodes of Al achieves the highest k_t^2, especially for h/λ lower than 0.06.

The operating principle of AlN-based lamb-wave resonators has been investigated by many researchers [8], [9], [12], [13], [31]–[34]. As illustrated in Fig. 5, the resonating structure can be treated as a suspended rectangular thin plate with an air boundary on two sides. The piezoelectric layer is sandwiched between top and bottom metal layers, in which either side could be IDT or floating metal. The design presented in this article is lateral field excitation (LFE) lamb wave CMRs with a floating bottom metal, which simplifies the fabrication process without etching via for top-bottom metal interconnection and minimizes the abnormal oriented grains (AOGs) during the AlN or AlScN film deposition. The electric field excited in the piezoelectric layer is primarily aligned along the film c-axis direction. The lamb wave is excited by top IDT electrodes with a wavelength λ in the lateral wave propagation direction. The piezoelectric thin film thickness h is designed as twice of wavelength λ_z in the vertical direction. CMRs mainly rely on d_{33} and d_{31} piezoelectric coefficients of AlScN layer, since λ and λ_z are not comparable, more specifically, λ is much larger than λ_z. The vibration mode of the CMRs is along the in-plane direction of the piezoelectric plate. As the thickness of AlScN thin films is fixed, resonant frequencies of CMRs can be defined by varying λ, as shown in Fig. 5(a). The fabrication procedure of demonstrated $Al_{0.78}Sc_{0.22}N$ CMRs is based on a process similar to previous work [4], [35], in which 200 nm Al interdigital electrodes (IDT) serves as top electrodes on the 500 nm suspended $Al_{0.78}Sc_{0.22}N$ thin films and 10 nm Ti/100 nm Pt floating metal serves as bottom electrodes. Devices h/λ (thickness of piezoelectric thin films versus length of the acoustic wave) are designed to range from 0.012 to 0.042. The same CMR devices based on 0.5 μm AlN thin film are also fabricated in order to compare the device performance. A high-quality $Al_{0.78}Sc_{0.22}N$ co-sputtering deposition and etching process using SiO_2 hard mask has been developed to fabricate the devices. Fig. 5 summarizes the fabrication steps. 10 nm Ti/100 nm Pt was

Authorized licensed use limited to: ShanghaiTech University. Downloaded on June 01,2023 at 08:48:10 UTC from IEEE Xplore. Restrictions apply.

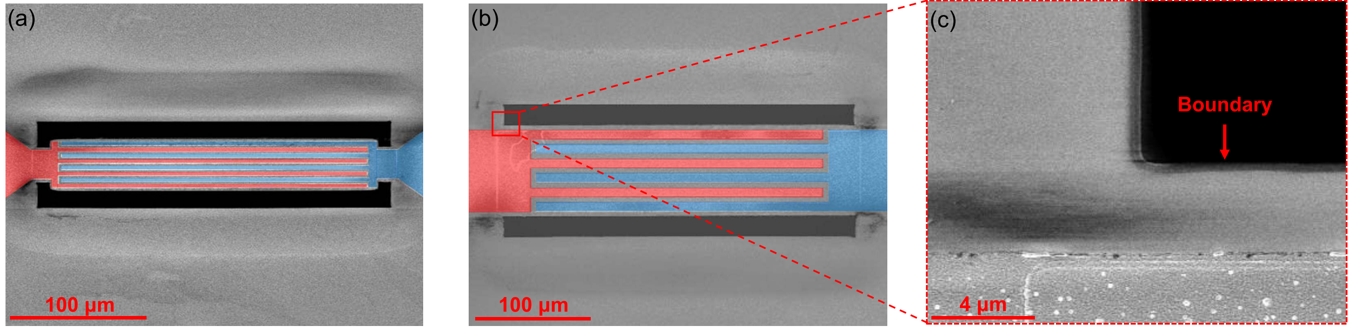

Fig. 6. SEM images of $Al_{0.78}Sc_{0.22}N$ CMRs with wavelength of (a) 12 μm and (b) 24 μm. (c) Top view of the zoom-in of Fig. 6(b) illustrates the boundary profile obtained by optimized $Al_{0.78}Sc_{0.22}N$ ICP etching recipe using SiO_2 hard mask.

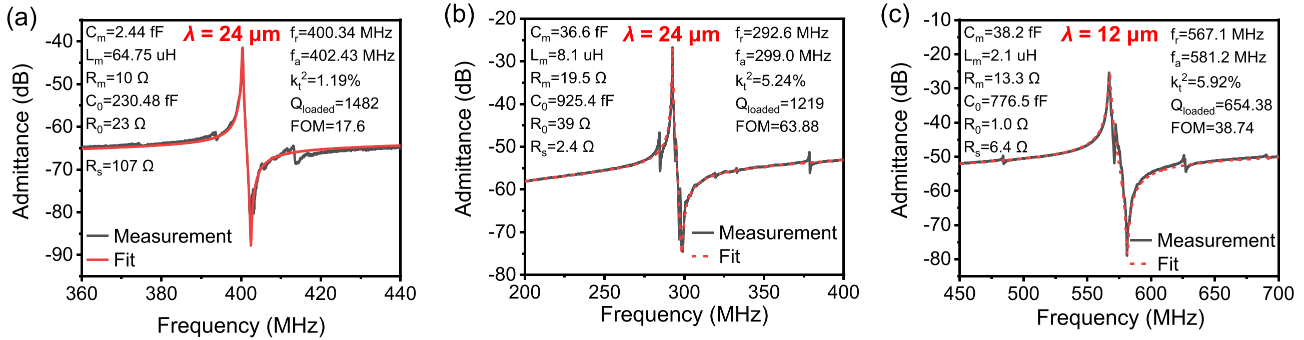

Fig. 7. Measured admittance response and MBVD fitting of (a) AlN CMR with wavelength of 24 μm, $Al_{0.78}Sc_{0.22}N$ CMRs with wavelength of (b) 24 μm, and (c) 12 μm.

first patterned on the high-resistive silicon wafer, followed by 0.5 μm $Al_{0.78}Sc_{0.22}N$ film deposition [see Fig. 5(b)–(g)]. A 2 μm SiO_2 hard mask was deposited and patterned as the AlScN etching mask, and then the AlScN film was etched to define the CMRs structure using ICP etching [see Fig. 5(d) and (e)]. A 200 nm Al layer was deposited and patterned as the top electrodes; finally, resonator devices were released by XeF_2, as shown in Fig. 5(f) and (g).

Fig. 6(a) and (b) shows the SEM images of the fabricated $Al_{0.78}Sc_{0.22}N$ CMRs. Fig. 6(a) illustrates the $Al_{0.78}Sc_{0.22}N$ CMR with eight aluminum IDT electrodes operating at about 570 MHz. Fig. 6(b) is an $Al_{0.78}Sc_{0.22}N$ CMR with six aluminum IDT electrodes working at about 290 MHz. Fig. 6(c) is the zoomed-in view of the etched boundary of the 290 MHz CMR. The steep profile is defined by $Al_{0.78}Sc_{0.22}N$ ICP etching using a SiO_2 hard mask. Although the etching rate of $Al_{0.78}Sc_{0.22}N$ is about 3× lower than that of AlN using a similar recipe, it allows successfully etching 500 nm $Al_{0.78}Sc_{0.22}N$ piezoelectric layer with a profile of 77°.

According to the above-mentioned simulations, we fabricate our $Al_{0.78}Sc_{0.22}N$ lamb wave CMRs with anchor length equal to 23 μm. Fig. 7(a)–(c) present the admittance response for the AlN CMR with a wavelength of 24 μm and $Al_{0.78}Sc_{0.22}N$ CMRs with a wavelength of 12 and 24 μm measured by Keysight[1] PNA-L N5234B network analyzer. The resonator equivalent electric parameters are extracted by fitting into the modified Butterworth-Van Dyke (mBVD) model [36] and are listed in the figures, where C_m, L_m, R_m are the motional capacitance, motional inductance, motional resistance of resonators, respectively, and R_s is the loaded resistance in series; C_0 and R_0 are the static capacitance and resistance of the resonator, respectively. As seen in Fig. 7(a), the AlN CMR with a similar device structure shows an electromechanical coupling coefficient of 1.19% and a quality factor of 1482 with an FoM of only 17.6. As shown in Fig. 7(b) and (c), the resonant frequencies are 292.6 and 567.1 MHz, respectively. For $Al_{0.78}Sc_{0.22}N$ CMR with a wavelength of 12 μm, the k_t^2 of 5.92% and quality factor Q of 654.38 are achieved, with an FoM value of 38.74. Thanks to the optimized $Al_{0.78}Sc_{0.22}N$ sputtering and etching process, as well as the optimal design of the devices, the best $Al_{0.78}Sc_{0.22}N$ CMR achieves k_t^2 of 5.24% and loaded Q of 1219, yielding a high FoM of 63.88 for 24 μm CMR. The measured quality factor of $Al_{0.78}Sc_{0.22}N$ CMR fits greatly with the theoretical result. The experimental k_t^2 of 5.24% shows perfect agreement with the predicted value obtained from the 2-D simulation. It is known that AlN-based FBAR and CLMR devices could achieve a higher FoM [37]. Therefore, utilizing our high quality and well stress-control AlScN thin film would generate even better performance.

Fig. 8(a) shows the electromechanical coupling coefficient k_t^2comparisons between measurement and FEA simulation of both $Al_{0.78}Sc_{0.22}N$ and AlN CMRs. The $Al_{0.78}Sc_{0.22}N$ CMRs experimental results agree with the simulation analysis greatly, with the best k_t^2 of approximately 6.2%, and the average value of 5.5%. The measured k_t^2 of $Al_{0.78}Sc_{0.22}N$ CMRs is about 3.2× higher than AlN CMRs. Fig. 8(b) shows the measured Q_{loaded} of $Al_{0.78}Sc_{0.22}N$ CMRs with a wavelength of 12 and 24 μm. The Q_{loaded} values of $Al_{0.78}Sc_{0.22}N$ CMRs with

Authorized licensed use limited to: ShanghaiTech University. Downloaded on June 01,2023 at 08:48:10 UTC from IEEE Xplore. Restrictions apply.

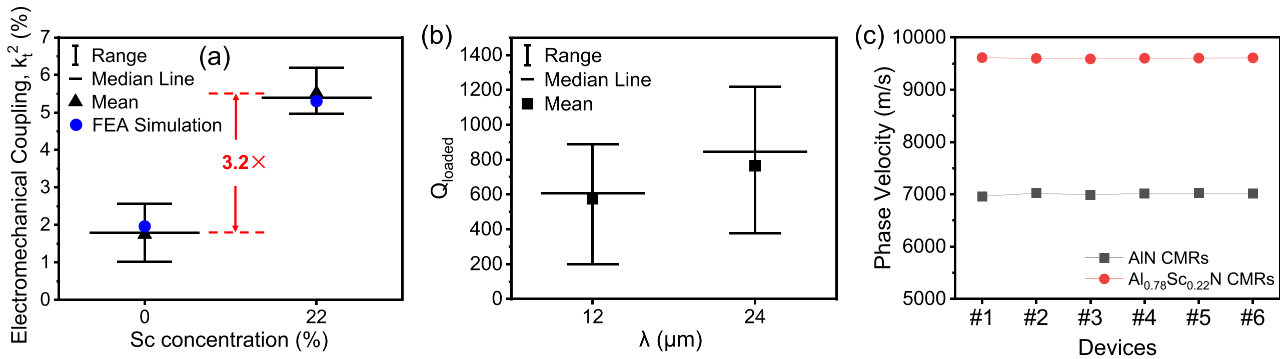

Fig. 8. (a) Comparison of electromechanical coupling coefficients in measured CMRs and FEA simulation based on AlN and $Al_{0.78}Sc_{0.22}N$ thin films. (b) Measured Q_{loaded} of $Al_{0.78}Sc_{0.22}N$ CMRs with wavelength of 12 and 24 μm. (c) Measured phase velocities of AlN and $Al_{0.78}Sc_{0.22}N$ CMRs.

TABLE I
COMPARISON OF PREVIOUS WORKS

Designs	Sc/%	Device	f_s /GHz	k_t^2/%	Q_{loaded}	FoM
[19]	12	LCAT	2.0	10.2	855	87.00
[38]	15	CMR	1.4	2.45	156	3.82
[15]	20	CMR	0.2	4.50	1240	55.80
[39]	20	CMR	2.7	5.64	540	30.46
[20]	30	CMR	0.3	7.74	1119	86.60
[40]	30	FBAR	2.9	18.1	210	38.00
[41]	40	CMR	2.6	7.39	117	7.71
This work	**22**	**CMR**	**0.3**	**5.24**	**1219**	**63.88**

24 μm are from 376.3 to 1219, while The Q_{loaded} values with 12 μm $Al_{0.78}Sc_{0.22}N$ CMRs are from 200 to 889. Due to more spurious modes in higher frequency, the Q_{loaded} values have a decreasing trend with increasing frequency. Fig. 7(c) shows the phase velocities of CMRs based on AlN and $Al_{0.78}Sc_{0.22}N$ films extracted by RF measurement. The phase velocity of AlN CMR operating at S_0 mode with a wavelength of 24 μm is about 9600 m/s, while that of $Al_{0.78}Sc_{0.22}N$ CMRs is about 7000 m/s. The reduction in phase velocity from pure AlN to $Al_{0.78}Sc_{0.22}N$ is because of the softening in the stiffness coefficient. The drop in phase velocity of S_0 mode decreases the operating frequency of devices.

The AlScN resonators are summarized and compared in Table I. Due to the high d_{33}, FBAR can achieve high k_t^2. However, it is challenging to achieve multi-resonance in one chip. Laterally coupled alternating thickness (LCAT) mode resonators usually obtained high k_t^2 by utilizing d_{31} and d_{33}, simultaneously. However, the fabrication process of LCAT resonators is much harder than CMRs, especially for working at high frequency (>1 GHz).

IV. CONCLUSION

In summary, the optimization of the deposition and etching process of $Al_{0.78}Sc_{0.22}N$ is demonstrated. About 22% Sc-doped co-sputtered AlScN thin films have been achieved with XRD FWHM of 1.8° and roughness RMS value of 1.40 nm. The $Al_{0.78}Sc_{0.22}N$ etching model is proposed and discussed. Using improved ICP dry etching method in fabrication, a vertical profile of 77° is obtained at $Al_{0.78}Sc_{0.22}N$ thin film, with a desirable etch rate of 130 nm/min, and selectivity of 1:1 relative to SiO_2 hard mask. In order to show that the optimized design of CMRs can improve the electromechanical coupling coefficient (k_t^2) and quality factor Q of resonators, several simulation results of $Al_{0.78}Sc_{0.22}N$ CMRs are discussed. The experimental results are constant with theoretical results. The CMRs based on AlN and $Al_{0.78}Sc_{0.22}N$ with varying wavelengths are fabricated and characterized. An $Al_{0.78}Sc_{0.22}N$ CMR operating at about 293 MHz with 5.24% k_t^2 and 1219 loaded Q, yielding a high FoM of 63.88, has been demonstrated. This result shows the improvement in the k_t^2 of more than 3.2× with respect to identical CMRs in pure AlN, operating with the same wavelength. Such a result encourages us to carry out further experiments to achieve the next generation of filters in RF applications.

REFERENCES

[1] T. Wu *et al.*, "Design and fabrication of AlN RF MEMS switch for near-zero power RF wake-up receivers," in *Proc. IEEE Sensors*, Oct. 2017, pp. 1–3.

[2] G. Piazza, P. J. Stephanou, and A. P. Pisano, "Piezoelectric aluminum nitride vibrating contour-mode MEMS resonators," *J. Microelectromech. Syst.*, vol. 15, no. 6, pp. 1406–1418, Dec. 2006.

[3] R. Ruby, "11E-2 review and comparison of bulk acoustic wave FBAR, SMR technology," in *Proc. IEEE Ultrason. Symp.*, Oct. 2007, pp. 1029–1040.

[4] A. Gao, K. Liu, J. Liang, and T. Wu, "AlN MEMS filters with extremely high bandwidth widening capability," *Microsyst. Nanoeng.*, vol. 6, no. 1, p. 74, Dec. 2020.

[5] J. G. Rodríguez-Madrid, G. F. Iriarte, J. Pedrós, O. A. Williams, D. Brink, and F. Calle, "Super-high-frequency SAW resonators on AlN/diamond," *IEEE Electron Device Lett.*, vol. 33, no. 4, pp. 495–497, Apr. 2012.

[6] G. Wingqvist, "AlN-based sputter-deposited shear mode thin film bulk acoustic resonator (FBAR) for biosensor applications—A review," *Surf. Coatings Technol.*, vol. 205, no. 5, pp. 1279–1286, Nov. 2010.

[7] J.-P. Jung, J.-B. Lee, M.-H. Lee, and J.-S. Park, "Experimental and theoretical investigation on the relationship between AlN properties and AlN-based FBAR characteristics," in *Proc. IEEE Int. Freq. Control Sympposium PDA Exhib. Jointly With 17th Eur. Freq. Time Forum*, Jan. 2003, pp. 779–784.

[8] S. I. Jung, C. Ryu, G. Piazza, and H. J. Kim, "A study on the effects of bottom electrode designs on aluminum nitride contour-mode resonators," *Micromachines*, vol. 10, no. 11, p. 758, Nov. 2019.

[9] M. Giovannini, S. Yazici, N.-K. Kuo, and G. Piazza, "Apodization technique for spurious mode suppression in AlN contour-mode resonators," *Sens. Actuators A, Phys.*, vol. 206, no. 1, pp. 42–50, Feb. 2014.

[10] Q.-X. Su, P. Kirby, E. Komuro, M. Imura, Q. Zhang, and R. Whatmore, "Thin-film bulk acoustic resonators and filters using ZnO and lead-zirconium-titanate thin films," *IEEE Trans. Microw. Theory Techn.*, vol. 49, no. 4, pp. 769–778, Apr. 2001.

Authorized licensed use limited to: ShanghaiTech University. Downloaded on June 01,2023 at 08:48:10 UTC from IEEE Xplore. Restrictions apply.

[11] L. Rana, R. Gupta, M. Tomar, and V. Gupta, "ZnO/ST-quartz SAW resonator: An efficient NO_2 gas sensor," *Sens. Actuators B, Chem.*, vol. 252, pp. 840–845, Nov. 2017.

[12] G. Piazza, P. J. Stephanou, and A. P. Pisano, "Single-chip multiple-frequency AlN MEMS filters based on contour-mode piezoelectric resonators," *J. Microelectromech. Syst.*, vol. 16, no. 2, pp. 319–328, Apr. 2007.

[13] S. Ghosh and G. Piazza, "Laterally vibrating resonator based elasto-optic modulation in aluminum nitride," *APL Photon.*, vol. 1, no. 3, Jun. 2016, Art. no. 036101.

[14] M. Park, Z. Hao, D. G. Kim, A. Clark, R. Dargis, and A. Ansari, "A 10 GHz single-crystalline scandium-doped aluminum nitride Lamb-wave resonator," in *Proc. 20th Int. Conf. Solid-State Sensors, Actuat. Microsyst. Eurosensors XXXIII (TRANSDUCERS EUROSENSORS XXXIII)*, Jun. 2019, pp. 450–453.

[15] L. Colombo, A. Kochhar, C. Xu, G. Piazza, S. Mishin, and Y. Oshmyansky, "Investigation of 20% scandium-doped aluminum nitride films for MEMS laterally vibrating resonators," in *Proc. IEEE Int. Ultrason. Symp. (IUS)*, Sep. 2017, pp. 1–4.

[16] L. Colombo, A. Kochhar, G. Vidal-Álvarez, and G. Piazza, "X-cut lithium niobate laterally vibrating MEMS resonator with figure of merit of 1560," *J. Microelectromech. Syst.*, vol. 27 no. 4, pp. 602–604, Aug. 2018.

[17] C. J. Sarabalis, T. P. McKenna, R. N. Patel, R. Van Laer, and A. H. Safavi-Naeini, "Acousto-optic modulation in lithium niobate on sapphire," *APL Photon.*, vol. 5, no. 8, Aug. 2020, Art. no. 086104.

[18] G. K. Fedder, C. Hierold, J. G. Korvink, and O. Tabata, *Resonant MEMS: Fundamentals, Implementation, and Application*, vol. 22. Hoboken, NJ, USA: Wiley, 2015.

[19] N. Wang *et al.*, "Over 10% of k^2_{eff} demonstrated by 2-GHz spurious mode-free $Sc_{0.12}Al_{0.88}N$ laterally coupled alternating thickness mode resonators," *IEEE Electron Device Lett.*, vol. 40, no. 6, pp. 957–960, Jun. 2019.

[20] S. Shao, Z. Luo, and T. Wu, "High figure-of-merit Lamb wave resonators based on $Al_{0.7}Sc_{0.3}N$ thin film," *IEEE Electron Device Lett.*, vol. 42, no. 9, pp. 1378–1381, Sep. 2021.

[21] M. Park, Z. Hao, R. Dargis, A. Clark, and A. Ansari, "Epitaxial aluminum scandium nitride super high frequency acoustic resonators," *J. Microelectromech. Syst.*, vol. 29, no. 4, pp. 490–498, Aug. 2020.

[22] L. Shu *et al.*, "The characterization of surface acoustic wave devices based on AlN-metal structures," *Sensors*, vol. 16, no. 4, p. 526, Apr. 2016.

[23] E. Yarar, V. Hrkac, C. Zamponi, A. Piorra, L. Kienle, and E. Quandt, "Low temperature aluminum nitride thin films for sensory applications," *AIP Adv.*, vol. 6, no. 7, Jul. 2016, Art. no. 075115.

[24] Y. R. Luo, *Comprehensive Handbook of Chemical Bond Energies*. Boca Raton, FL, USA: CRC Press, 2007.

[25] M.-A. Dubois and P. Muralt, "Stress and piezoelectric properties of aluminum nitride thin films deposited onto metal electrodes by pulsed direct current reactive sputtering," *J. Appl. Phys.*, vol. 89, no. 11, pp. 6389–6395, Jun. 2001.

[26] Z. Luo, S. Shao, and T. Wu, "Characterization of AlN and AlScN film ICP etching for micro/nano fabrication," *Microelectron. Eng.*, vols. 242–243, Apr. 2021, Art. no. 111530.

[27] G. Chen, F. Pop, and M. Rinaldi, "Super high frequency lateral-field-excited aluminum nitride cross-sectional Lamé mode resonators," in *Proc. 20th Int. Conf. Solid-State Sensors, Actuat. Microsyst. Eurosensors XXXIII (TRANSDUCERS EUROSENSORS XXXIII)*, Jun. 2019, pp. 539–542.

[28] M. A. Caro *et al.*, "Piezoelectric coefficients and spontaneous polarization of ScAlN," *J. Phys., Condens. Matter*, vol. 27, no. 24, Jun. 2015, Art. no. 245901.

[29] Y.-Y. Chen, Y.-T. Lai, and C.-M. Lin, "Finite element analysis of anchor loss in AlN Lamb wave resonators," in *Proc. IEEE Int. Freq. Control Symp. (FCS)*, May 2014, pp. 1–5.

[30] B. P. Harrington and R. Abdolvand, "In-plane acoustic reflectors for reducing effective anchor loss in lateral–extensional MEMS resonators," *J. Micromech. Microeng.*, vol. 21, no. 8, Jul. 2011, Art. no. 085021.

[31] J. Zou, C.-M. Lin, A. Gao, and A. P. Pisano, "The multi-mode resonance in AlN Lamb wave resonators," *J. Microelectromech. Syst.*, vol. 27, no. 6, pp. 973–984, Dec. 2018.

[32] G. Piazza, P. J. Stephanou, and A. P. Pisano, "One and two port piezoelectric higher order contour-mode MEMS resonators for mechanical signal processing," *Solid-State Electron.*, vol. 51, nos. 11–12, pp. 1596–1608, 2007.

[33] M. Rinaldi, C. Zuniga, C. Zuo, and G. Piazza, "Super-high-frequency two-port AlN contour-mode resonators for RF applications," *IEEE Trans. Ultrason., Ferroelectr., Freq. Control*, vol. 57, no. 1, pp. 38–45, Jan. 2010.

[34] C. Cassella, Y. Hui, Z. Qian, G. Hummel, and M. Rinaldi, "Aluminum nitride cross-sectional lam? Mode resonators," *J. Microelectromech. Syst.*, vol. 25, no. 2, pp. 275–285, Apr. 2016.

[35] G. Piazza, V. Felmetsger, P. Muralt, R. H. Olsson, III, and R. Ruby, "Piezoelectric aluminum nitride thin films for microelectromechanical systems," *MRS Bull.*, vol. 37, no. 11, pp. 1051–1061, Nov. 2012.

[36] J. D. Larson, P. D. Bradley, S. Wartenberg, and R. C. Ruby, "Modified butterworth-van dyke circuit for FBAR resonators and automated measurement system," in *Proc. IEEE Ultrason. Symp. Int. Symp.*, Oct. 2000, pp. 863–868.

[37] C. Cassella, G. Chen, Z. Qian, G. Hummel, and M. Rinaldi, "RF passive components based on aluminum nitride cross-sectional Lamé-mode MEMS resonators," *IEEE Trans. Electron Devices*, vol. 64, no. 1, pp. 237–243, Jan. 2017.

[38] F. Parsapour *et al.*, "Free standing and solidly mounted Lamb wave resonators based on Al0.85Sc0.15N thin film," *Appl. Phys. Lett.*, vol. 114, no. 22, Jun. 2019, Art. no. 223103.

[39] Z. A. Schaffer, G. Piazza, S. Mishin, and Y. Oshmyansky, "Super high frequency simple process flow cross-sectional Lamé mode resonators in 20% scandium-doped aluminum nitride," in *Proc. IEEE 33rd Int. Conf. Micro Electro Mech. Syst. (MEMS)*, Jan. 2020, pp. 1281–1284.

[40] J. Wang, M. Park, S. Mertin, T. Pensala, F. Ayazi, and A. Ansari, "A film bulk acoustic resonator based on ferroelectric aluminum scandium nitride films," *J. Microelectromech. Syst.*, vol. 29, no. 5, pp. 741–747, Oct. 2020.

[41] A. Konno *et al.*, "ScAlN Lamb wave resonator in GHz range released by XeF_2 etching," in *Proc. IEEE Int. Ultrason. Symp. (IUS)*, Jul. 2013, pp. 1378–1381.

Zhifang Luo (Student Member, IEEE) received the B.S. degree in physics from ShanghaiTech University, Shanghai, China, in 2019, where he is currently pursuing the Ph.D. degree in electrical engineering.

His research interests include the design and microfabrication techniques of piezoelectric microelectromechanical system (MEMS) resonators for RF and sensing applications and hybrid microsystems based on the integration of MEMS devices with photonics for signal processing.

Shuai Shao received the B.S. degree in electrical engineering from Xidian University, Xi'an, China, in 2018. He is currently pursuing the Ph.D. degree with ShanghaiTech University, Shanghai, China.

His research interest includes the design and microfabrication techniques of microelectromechanical system (MEMS) resonators for radio frequency microsystems.

Tao Wu (Member, IEEE) received the B.S. degree (Hons.) in electrical engineering from Zhejiang University, Hangzhou, China, in 2007, and the M.S. and Ph.D. degrees from the University of California at Los Angeles, Los Angeles, CA, USA, in 2009 and 2011, respectively.

He was a Process TD Engineer with Intel Corporation, Hillsboro, OR, USA, from 2012 to 2014. Then, he held a Postdoctoral Researcher Fellow position at Stanford University, Stanford, CA, USA, and Northeastern University, Boston, MA, USA, from 2014 to 2017. He is currently an Assistant Professor with the School of Information Science and Technology, ShanghaiTech University, Shanghai, China. He has authored or coauthored more than 60 papers in prestigious IEEE journals and conferences. His research interests include the design and fabrication of multiferroic transducers, piezoelectric resonators, and integrated circuit for microelectromechanical system (MEMS)-based microsystems.

Authorized licensed use limited to: ShanghaiTech University. Downloaded on June 01,2023 at 08:48:10 UTC from IEEE Xplore. Restrictions apply.